MULTI-MISSION EARTH ENTRY VEHICLE SUBSONIC DYNAMIC STABILITY TESTING AND ANALYSES

Louis Glaab[(1)] and C. Michael Fremaux[(2)]

[(1)]Atmospheric Flight and Entry Systems Branch, NASA Langley Research Center
[(2)]Flight Dynamics Branch, NASA Langley Research Center

ABSTRACT

Multi-Mission Earth Entry Vehicles (MMEEVs) are blunt-body vehicles designed with the purpose of transporting payloads from space to the surface of the Earth. To achieve high reliability and minimum weight, MMEEVs avoid using limited-reliability systems, such as parachutes, retro-rockets, and reaction control systems. Multi-Mission Earth Entry vehicles rely on the natural aerodynamic stability of the vehicle throughout the Entry, Descent, and Landing phase of flight.

Testing in NASA Langley's Vertical Spin Tunnel (VST) was conducted to improve subsonic aerodynamic models of this class of vehicle. As the center of mass of a vehicle moves aft, due to placement of components or other design aspects, its' stability is decreased resulting in larger amplitude oscillations and reduced ability to recover from atmospheric disturbances resulting from turbulence. Design requirements for effective impact attenuation involve maximum attitude limits. Vehicle reliability requirements influence the vehicle's ability to recover from atmospheric disturbances. The objectives of the VST testing were to define usable subsonic center of mass limits to meet potential design requirements, and aerodynamic parameters for 6-degree-of-freedom (6-DOF) simulations, for a range of MMEEV designs. This report documents the resulting data from the initial VST test that used a 1.8m MMEEV. Results indicate that the 1.8m MMEEV is stable for the conditions tested which included center of mass at 0.214D and 0.234D and with nominal and 150% moment of inertias. Subsequent testing, planned for 2013, will include a 1.2m MMEEV along with provisions of testing an enlarged backshell.

1. SYMBOLS AND ACRONYMS

6-DOF	6-degree-of-freedom
C_i	Aero equation coefficients (C_0, C_1, C_2, etc.).
C_A	Axial force coefficient
C_l	Rolling moment coefficient
C_m	Pitching moment coefficient
C_n	Yawing moment coefficient
C_N	Normal force coefficient
C_Y	Side force coefficient
CM	Center of Mass
D	Model and Full-Scale diameter
I_{XX}	Model moment inertia about X axis
I_{YY}	Model moment inertia about Y axis
I_{ZZ}	Model moment inertia about Z axis
l_m	Model length
l_v	Full-scale vehicle length
MMEEV	Multi-Mission Earth Entry Vehicle
M-SAPE	Multi-Mission System Analysis for Planetary Entry tool
MSPS	Model Space Positioning System
MSR	Mars Sample Return
n	Number of runs in a Block
N	Ratio of model to full-scale size
$\hat{p}$	Non-dimensional roll rate
PID	Parameter IDentification
$\hat{q}$	Non-dimensional pitch rate
$\hat{r}$	Non-dimensional yaw rate
Re	Reynolds number
Rx, Ry, Rz	Euler angles (x-y-z rotation sequence)
ρ_m	Model air density
ρ_V	Full scale vehicle air density
TPS	Thermal Protection System
ν_m	Model velocity
ν_v	Full scale vehicle velocity
V_∞	Model total airspeed
VST	NASA LaRC Vertical Spin Tunnel
ψ, θ, ϕ	Standard aerospace Euler angles (z-y-x rotation sequence)
x, y, z	Wind tunnel model axis system
X, Y, Z	VST axis system
ξ_A	Distance of model motion reference center from the cone apex
ξ_N	Distance of model motion reference center from the actual nose of the vehicle

2. INTRODUCTION

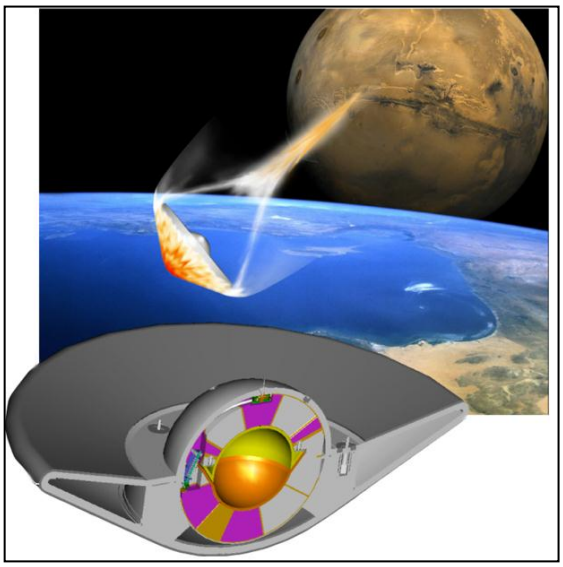

Figure 1 – Mars Sample Return concept (NASA Graphic)

Multi-Mission Earth Entry Vehicles (MMEEVs) are designed to transport payloads from outside of the atmosphere to the surface of the Earth. They serve as the last leg of missions to gather samples from around the solar system for detailed analysis on Earth. Multi-Mission Earth Entry Vehicles can have various sizes, shapes, designs, and concept of operations that reflect unique mission requirements. In general, however, many of the prior and planned future MMEEVs can be viewed as a class of vehicle with many similar characteristics. Multi-Mission Earth Entry Vehicles have high speeds resulting from direct atmospheric entries. In addition, many MMEEVs are single-stage entry concepts that do not include parachutes, retro-rockets, or reaction control systems for example, in order to minimize complexity and weight while maximizing reliability. At landing the remaining kinetic energy is dissipated by built-in energy absorption systems as described in [1]. Figure 1 illustrates a NASA-LaRC concept for a Mars Sample Return (MSR) Earth Entry Vehicle, which is considered to be a member of the family of MMEEVs.

To assess vehicle designs for multiple missions, as well as develop advanced integrated multi-disciplinary automated design tools, the Multi-Mission Systems Analysis for Planetary Entry (M-SAPE) tool [2] is being developed. It is used to facilitate the design of MMEEVs for an array of missions and develop and visualize the trade space. The M-SAPE tool improves and speeds up the design activities such as trade studies, sensitivity analyses, Monte Carlo analyses, and vehicle optimization.

During the final minutes of descent, MMEEVs will be flying at subsonic Mach conditions. Shapes designed to optimize aerothermal heating, such as large angle blunted cones, can possess limited usable center-of-mass (CM) ranges due to subsonic static and dynamic aerodynamic stability issues [3]. Depending on the mission, payload mass and density, entry trajectory, and payload impact and temperature requirements, MMEEVs can have varying overall diameters and backshell sizes.

The M-SAPE program requires a data base to support its system engineering functions and adequately model outer moldline variations for a range of MMEEV designs. For low-fidelity analyses, an approximate range of usable CMs for a family of MMEEVs designs is desired. Higher-fidelity 6-degree-of-freedom (6-DOF) simulation analyses also require an accurate aerodynamic database. Currently, the aerodynamic models used for M-SAPE are based on a combination of computational fluid dynamics and wind-tunnel data for similar entry vehicles. Subsonic aerodynamic models were based on data from [3, 4] combined with dynamic aerodynamic data obtained from the Viking program [5].

The current effort was performed to improve the subsonic aerodynamic modeling capability of the M-SAPE tool as well as to provide a comprehensive low-speed aero database for MMEEVs. A representative MMEEV wind tunnel model was fabricated and tested in the NASA LaRC 2-Foot Vertical Spin Tunnel (VST). This model was dynamically scaled to represent the full-scale MMEEV.

3. APPARATUS

3.1. Wind Tunnel

The dynamic stability tests were performed in the Langley VST. The VST is a sea-level atmospheric, low-speed, annular return tunnel with a closed, twelve-sided test section that is 20 feet (6.1 m) wide and 25 feet (7.6 m) long. The maximum tunnel dynamic pressure is approximately 9 lb/ft^2 at a speed of 87 ft/s (Re= 550,000 per foot). For the current test, the average dynamic pressure was approximately 1.7 lb/ft^2. The resulting Reynolds number based on model maximum diameter was approximately 0.24x10^6. The fan drive control is designed to provide rapid acceleration and deceleration of the flow (+15 ft/s^2 and -25 ft/s^2, respectively) through a joystick controller so that a model may be kept (vertically) in the designated test volume. A lightweight "safety tether" system can be used to minimize model damage due to impact with the test-section walls and reduce test time when appropriate. See Figure 2 for a cross sectional sketch of the facility.

Upper and lower nets prevent models from getting drawn into the fan or falling through the flow straightening honeycomb. The test section walls are padded to minimize model damage due to impact, but a safety tether was used during most of these tests in order to further reduce the likelihood of model damage. The tether consists of a lightweight braided nylon line attached to the model with a ball-bearing swivel. It was

kept slack during data runs, but was tightened to prevent the model from impacting the wind tunnel walls by an operator using an electric winch.

A method to excite or perturb the models is also part of the VST test capability. Essentially the perturbation method is a long pole with a padded end. One of the tunnel operators can contact the model with the perturbation pole to induce approximate model responses.

A series of cameras around the test section provide video coverage as input to an optical data acquisition system (to be discussed in the next section). The VST has been used for studying the spin characteristics of aircraft (hence the name of the tunnel), however, there have also been numerous dynamic stability tests for atmospheric entry vehicles. Among the entry vehicles tested are Mercury [6], Gemini [7], Apollo [8], Pioneer Venus [9] and Stardust [10].

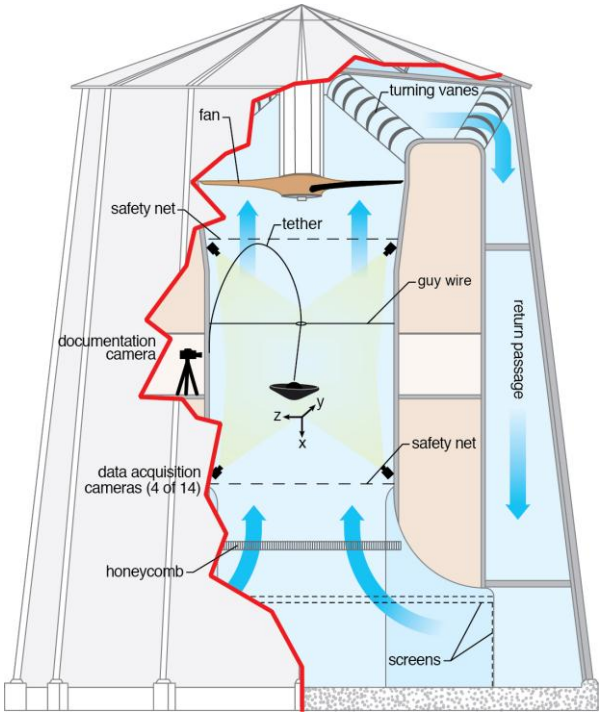

Figure 2 Cross-section of 20-Foot Vertical Spin Tunnel

3.2. Data Acquisition System

An optical data acquisition system is used to obtain 6-DOF motion time histories of models during dynamic tests. The VST Model Space Positioning System, or MSPS [11], is a non-intrusive, workstation-based system that eight digital cameras to image a pattern of retro-reflective targets on a model to generate post-test estimates of model attitude (ψ, θ, ϕ) and spatial position (X, Y, Z) with respect to an earth-fixed test section axis system (Figure 2) at a sample rate of 150 Hz using near-infrared LEDs as a light source. At the start of data acquisition, test section state (dynamic pressure, flow velocity, temperature) are recorded on a separate system and time-correlated for post-test processing. Numerical differentiation of the attitude time histories is used to calculate angular rates. Comparisons to a reference at known attitudes indicate that angles reported by MSPS are accurate to within ±0.2 degrees.

3.3. MMEEV Model

The initial VST tunnel entry was performed using a dynamically scaled model of a 1.8m (5.91 ft) MMEEV that was designed to carry a 25 kg payload with a payload density of 4,000 kg/m^3. The thermal protection system selected for this design was Phenolic Impregnated Carbon Ablator material. The 1.8m MMEEV was a 60 degree sphere-cone design with a full-scale diameter of 1.8m. The nose and shoulder radii were 0.173D and 0.029D, respectively. The full-scale mass characteristics are provided in Table 1.

Table 1 – Full-scale characteristics

Configuration	Mass (kg)	I_{XX} (kg-m^2)	I_{YY} (kg-m^2)	I_{ZZ} (kg-m^2)
Baseline	83.66	21.268	12.331	12.294
Aft CM	83.43	21.268	12.687	12.674
Aft CM+150% inertias	84.21	32.505	17.947	17.852

Definition of the required model scale characteristics were based on the methods in [12]. For this scaling process, Froude number and relative density similitude are required between model and vehicle to obtain dynamic similarity. The scaling factors are provided in Table 2. The subscript "m" stands for model and "v" for full-scale.

Table 2 - Model scaling factors

Parameter	Scale Factor (Model/Full-Scale)
Linear Dimension	$N = \ell_m / \ell_v$
Relative Density	1
Froude Number	1
Mass	$N^3 \rho_m/\rho_v$
Moment of Inertia	$N^5 \rho_m/\rho_v$
Linear Velocity	$N^{1/2}$
Linear Acceleration	1
Angular Velocity	$1/N^{1/2}$
Time	$N^{1/2}$
Reynolds Number	$N^{3/2} \nu_m/\nu_v$

A scale model size of 1 ft (0.3048 m) was selected for this test which is similar in size to previous capsule-style models tested in the VST. The resulting model size was 16.93% of full-scale. The corresponding model scale mass characteristics are provided in Table 3. The products of inertia were zero, reflecting a CM along the model centerline. The CM location was

measured from the forward surface (nose) of the model and not the theoretical apex. For this VST test, data were acquired for model configurations for a forward CM (0.214D), where D is the maximum diameter of the model as well as for an aft CM location (0.234D) measured from the actual nose of the vehicle. In order to explore the effects of inertia for this type of vehicle, the model inertias tested were the nominal configuration as well as 150% of nominal. Testing over a range of CMs and inertias provided some coverage for a range of MMEEV designs that are similar to the 1.8m MMEEV outer mold line.

Table 3 - Model characteristics

Configuration	Mass (kg)	Ixx (kg-m^2)	Iyy (kg-m^2)	Izz (kg-m^2)
CM=0.214D	0.473	0.003468	0.002012	0.001999
CM=0.234D	0.474	0.003457	0.002061	0.002074
CM=0.234D +150% inertias	0.476	0.005287	0.002915	0.002901

The model was constructed out of polycarbonate material and manufactured using an additive manufacturing process. For this manufacturing process, the models were essentially "printed" from a machine using 3-D design software. Once removed from the additive manufacturing machine, the models required some sanding and painting. The reflective targets were then added with their locations precisely recorded with respect to the model reference point. Top and bottom views of the model are provided in Figures 3 and 4, respectively. The model reference coordinate system is presented in Figure 5, which shows the motion reference center in relation to both the actual nose of the vehicle and the theoretical apex. The motion reference center, ξ_N, was set to 2.139" and 2.377" for 0.214D and 0.234D CMs, respectively. The CM was located on the model centreline.

Figure 3 – Top view of 1.8m MMEEV model.

Figure 4 - Bottom view of 1.8m MMEEV model.

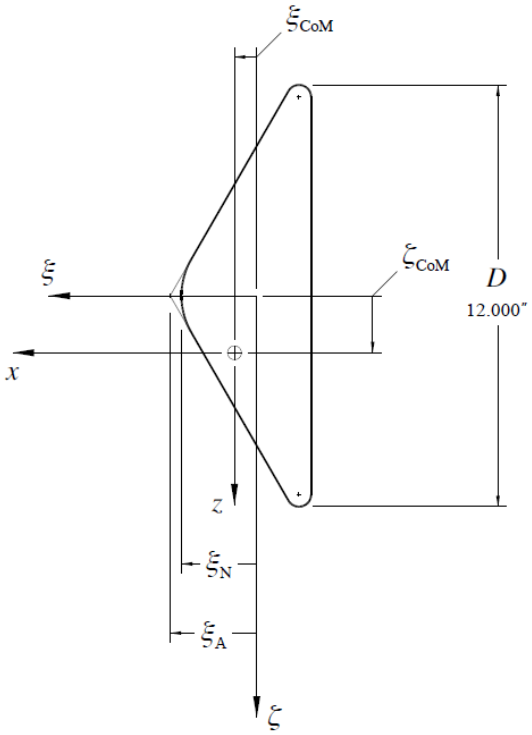

Figure 5 - Model coordinate reference system

4. EXPERIMENTAL MATRIX

Testing in the VST is performed in blocks of runs. Runs within a block are repeat runs of that condition. The runs were blocked by whether the model was tethered (T) or untethered (UT), perturbed (P) or unperturbed (UP) and by the configuration of the model. For each tethered model configuration, unperturbed and perturbed data were acquired. For the unperturbed data, the model was allowed to oscillate in the tunnel for approximately one minute for each run. The perturbations included model attitudes of approximately 20 to 70 degrees. This level of perturbation is valuable to evaluate the ability of the design to recover from extreme attitudes as well as to provide aerodynamic data for large angles of attack. The definition of each block of runs, along with the numbers of runs (n) in each block, are listed in Table 4.

Table 4 - 1.8m MMEEV Test Matrix

Block	T	UT	UP	P	CM	Inertias	n
1	Y		Y		0.214D	Nom	4
2	Y			Y	0.214D	Nom	15
3	Y		Y		0.234D	Nom	4
4	Y			Y	0.234D	Nom	8
5	Y		Y		0.234D	1.5*Nom	5
6	Y			Y	0.234D	1.5*Nom	1
7		Y	Y		0.214D	Nom	3

5. DATA ANALYSES AND RESULTS

For this report the data are presented in terms of total angle of attack for a block of runs for the full-scale vehicle. The simulated altitude for the data presented is 5,000 ft (~1,524 m). In addition, some preliminary results from an aerodynamic parameter identification (PID) effort are presented at model scale and sea-level conditions.

5.1. Time history data

CM 0.214D, nominal inertias: Figure 6 provides total angle of attack for a 12 second period. Three runs from Block-1 are presented. The time indices of data were adjusted in an attempt to align the peaks and troughs in the data for improved visibility. As can be seen in Figure 6 the peak total angle of attack was approximately 11 degrees. Most of the results from Figure 6 indicate that the vehicle was in an oscillatory limit cycle with maximum total angle of attack was between 5 and 10 degrees.

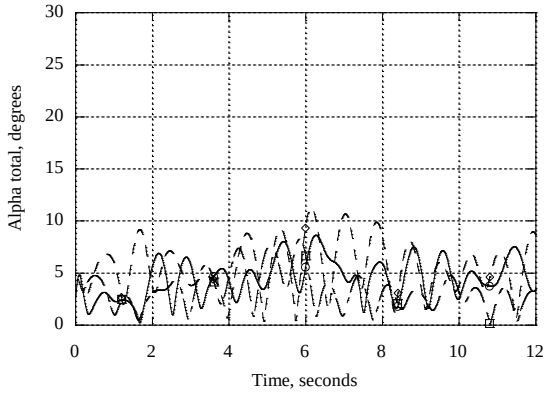

Figure 6 - Total angle of attack vs. time, CM=0.214D, unperturbed.

Perturbed results for the 0.214D CM condition are presented in Figure 7 for a time of 20 seconds. For these results the model was perturbed to generate total angles of attack up to 70 degrees. Results in Figure 7 indicate that even at these large angles of attack the vehicle is dynamically stable and returned back to a total angle of attack range between 10 and 20 degrees.

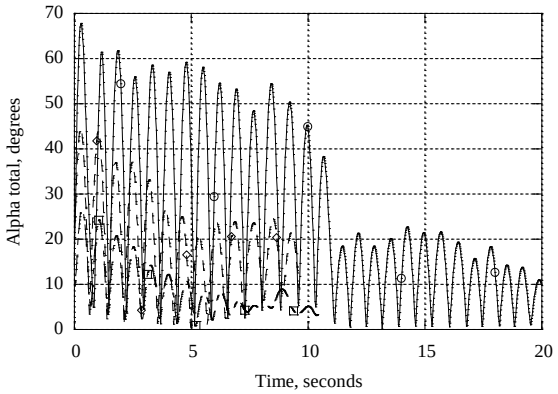

Figure 7 - Total angle of attack vs. time, CM=0.214D, perturbed.

CM 0.234D, nominal inertias: Total angle of attack results for the aft CM condition are presented in Figure 8. These results indicate that the effect of the aft CM was to increase the peak total angles of attack for the unperturbed limit cycle to be from approximately 7 to 15 degrees.

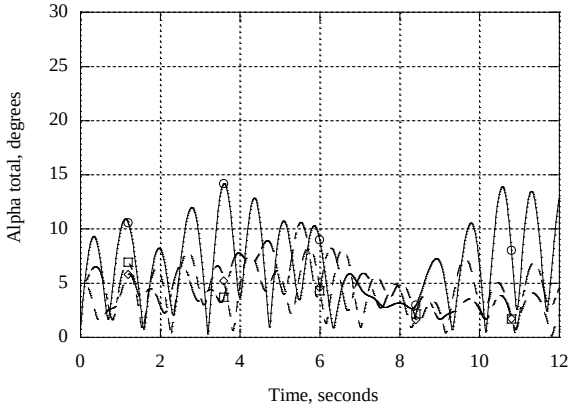

Figure 8 - Total angle of attack vs. time, CM = 0.234D, unperturbed.

Results for the perturbed 0.234D CM configuration are presented in Figure 9, the model was perturbed up to 55 degrees total angle of attack. As was the case for the 0.214D CM, the 0.234D CM results indicate that the oscillation amplitude decreased over approximately 10 seconds to become similar to the unperturbed maximum total angles of attack. Comparing Figure 6 (0.214 CM) with Figure 8 (0.234 CM) it can be seen the effect of moving the CM back 0.02D yielded an 8 degree change in the peak total angle of attack limit cycle oscillation. By comparing the perturbed results for the 0.214D and 0.234D conditions in Figures 7 and 9 indicate similar damping for the aft CM condition. Based on the results for total angle of attack, it would be expected that the 1.8m MMEEV simulated by these data would have acceptable attitude performance and impact the ground with maximum total angles of attack of less than 15 degrees for the 0.214D and 0.234D CMs with nominal inertias.

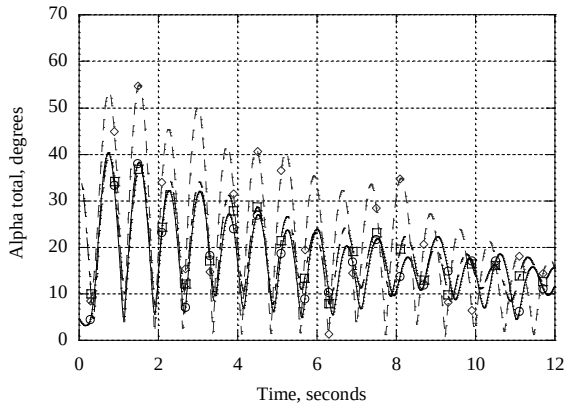

Figure 9 - Total angle of attack vs. time, CM=0.234D, perturbed.

CM 0.234D, 150% inertias: The effect of increased inertia for the aft CM can be seen in Figure 10 for the unperturbed block. As can be seen from comparison of Figures 10 (150% inertias) and 8 (baseline inertias) the maximum total angle of attack was increased by approximately 10 degrees. While exact maximum required impact angles have not been defined for the MMEEV, the large amplitude limit cycles for the 150% condition could create problems for payload impact dynamic g-limit requirements.

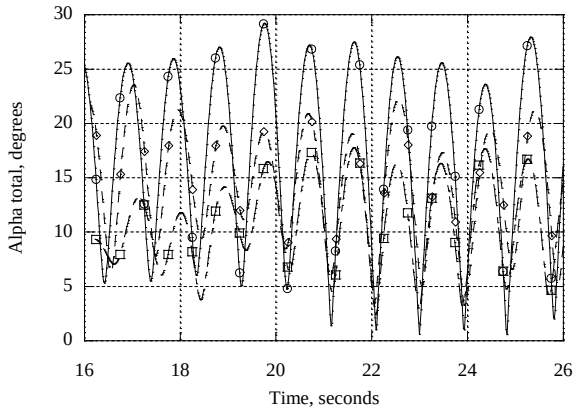

Figure 10 - Total angle of attack vs. time, CM=0.234D 150% inertias, unperturbed.

Only one run was performed for the perturbed 150% inertia 0.234D CM condition (Block 6). Unfortunately, the magnitude of the perturbation for this run did not exceed the maximum limit cycle maximum total angle of attack for this model configuration. As a result it is unclear if the vehicle is dynamically stable for maximum total angles of attack greater than ~25 degrees.

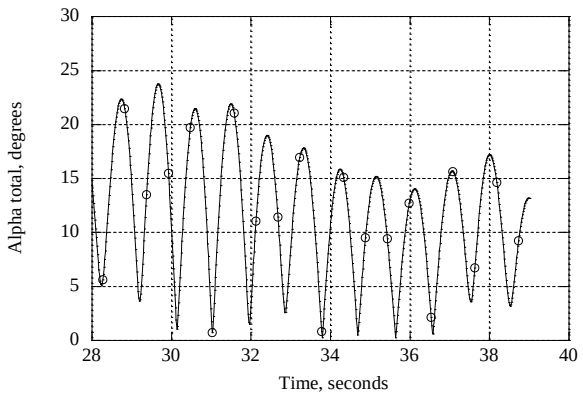

Figure 11 - Total angle of attack vs. time, CM=0.234D 150% inertias, perturbed.

5.2. PID analysis and results

Parameter Identification (PID) techniques were applied in an effort to identify aerodynamic coefficients for use in 6-DOF simulations. Preliminary results are presented herein using the methods and techniques as described in [13]. Parameter identification is often referred to as Aircraft System Identification. System identification is defined as the determination, on the basis of observation of input and output, of a system within a specified class of systems to which the system under test is equivalent [13].

For the PID analysis, time, model position (X, Y, and Z) and model orientation (R_x, R_y, and R_z) were used. Model orientation angles, R_x, R_y, and R_z, are similar to Euler angles, however, the sequence of rotation is altered (i.e., X-Y-Z sequence) to avoid singularities associated with the nearly vertical flight path experienced with VST testing. The first step in the PID process is to generate experimental aerodynamic coefficients as a function of time using equations of motion adapted to the VST free flight test techniques. The second part uses the least squares method as defined in Reference 14 to identify coefficients to equations to model the experimental data.

The aerodynamic coefficient models used for the PID analysis are provided below. Note that the various coefficients, C_0, C_1, C_3, C_4, are unique to each aerodynamic coefficient. A constant term is used in each equation to account for small asymmetries and data biases except for the axial force coefficient. The VST MMEEV model was symmetric about the longitudinal axis. Including a constant term provides the ability to account for experimental biases that could be due to wind tunnel flow or model symmetry factors, among other things. In general, the constant terms are checked to ensure that their magnitudes are an order of magnitude smaller compared to the effects from the other coefficients. The aerodynamic coefficient models were defined to replicate the data distributions from references [e.g. 3, 4, 5, 6].

Axial Force, C_A:

$$C_A = C_0 \times \cos(\propto) \quad \text{(eq 5.2.1)}$$

Normal Force, C_N:

$$C_N = C_0 + C_1 \times \sin(\propto) + C_2 \times \sin(\propto)^3 \quad \text{(eq 5.2.2)}$$

Side Force, C_Y:

$$C_Y = C_0 + C_1 \times \sin(\beta) + C_2 \times \sin(\beta)^3 \quad \text{(eq 5.2.3)}$$

Pitching moment, C_m:

$$C_m = C_0 + C_1 \times \propto + C_2 \times \hat{q} + C_3 \times \hat{q} \times \propto^2 \quad \text{(eq 5.2.4)}$$

Yawing moment, C_n:

$$C_n = C_0 + C_1 \times \beta + C_2 \times \hat{r} + C_3 \times \hat{r} \times \beta^2 \quad \text{(eq 5.2.5)}$$

Rolling moment, C_l:

$$C_l = C_0 + C_1 \times \hat{p} + C_2 \times \dot{\hat{p}} \quad \text{(eq 5.2.6)}$$

Where:

$$\hat{q} = \left(\frac{q+\dot{\alpha}}{2}\right) * D/(2 * V_\infty) \quad \text{(eq 5.2.7)}$$

$$\hat{r} = \left(\frac{r+\dot{\beta}}{2}\right) * D/(2 * V_\infty) \quad \text{(eq 5.2.8)}$$

$$\hat{p} = \left(\frac{p}{2}\right) * D/(2 * V_\infty) \quad \text{(eq 5.2.9)}$$

$$\dot{\hat{p}} = \left(\frac{\dot{p}}{2}\right) * D/(2 * V_\infty) \quad \text{(eq 5.2.10)}$$

Due to schedule constraints, only initial results from the PID analysis are presented herein to demonstrate the capability. Plans are to analyse the entire data set to generate a parametric subsonic MMEEV aerodynamic model.

Figure 12 shows a comparison of the resulting model data to the experimental normal force coefficient, C_N for one of the baseline unperturbed forward CM data runs. Given the definition of the PID model, C_N is only a function of angle of attack. As a result, only a single line is defined for all of the angle of attack range. The experimental data falls along and around the model line.

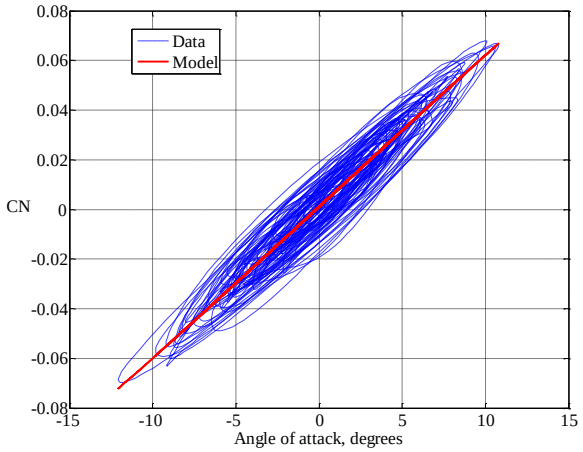

Figure 12 - C_N vs angle of attack, B1R2.

Figure 13 shows time history data for both the experimental data and the PID model. From this figure it can be seen that the model does effectively replicate the characteristics of the experimental data. However, some of the peaks in the experimental data are not replicated in the model data.

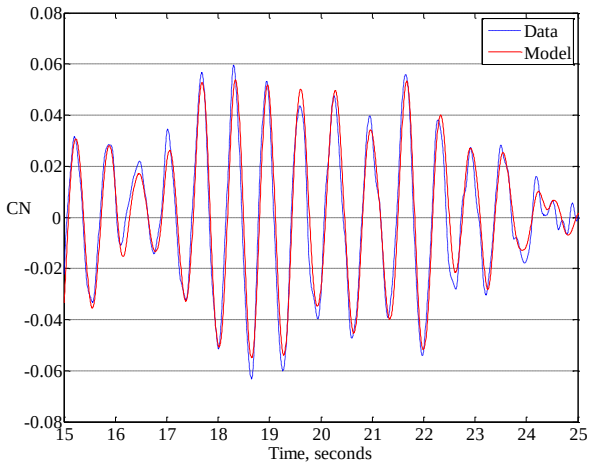

Figure 13 - C_N vs. time, B1R2.

Results for pitching moment, C_m are presented in Figure 14 vs angle of attack. For this coefficient, the model is a function of angle of attack as well as non-dimensional pitch rate, $\hat{q}$, and the product of $\hat{q}* \alpha^2$. Including $\hat{q}$, and $\hat{q}* \alpha^2$ in the pitching moment model equation leads to a range of values for C_m for specific angles of attack as can be seen in Figure 14.

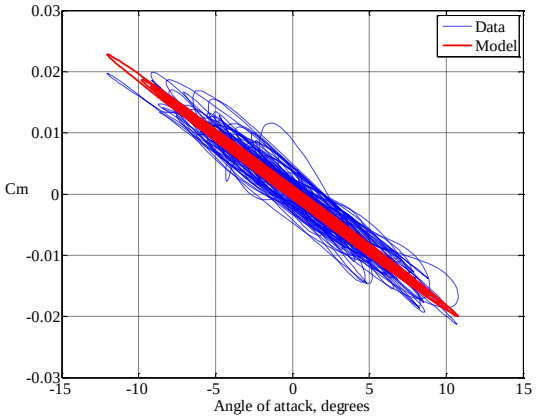

Figure 14 - Cm vs. angle of attack, B1R2.

Time history data comparison of the pitching moment experimental data with the model data is shown in Figure 15. As was the case for the normal force coefficient, there is good agreement between the experimental data and model. However, the model does not match some of the data peaks.

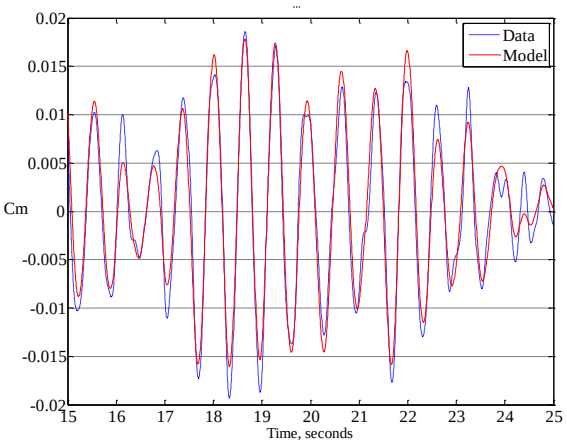

Figure 15 - Cm vs. time, B1R2.

The resulting coefficients for equations 5.2.1 through 5.2.6 are presented in Table 5 for this PID example taken from the Block 1 Run 2 (i.e. run B1R2). Note that these equations were defined for data over a range of approximately -10 to 10 degrees angle of attack. The perturbed data runs provide significantly greater angle of attack range for this data analysis.

Table 5 - Resulting PID equation coefficients

	C_0	C_1	C_2	C_3	Eq
C_A	0.836				5.2.1
C_N	0.0011	0.3519	-0.0681		5.2.2
C_Y	-0.003	-0.3603	-0.1912		5.2.3
C_m	0.0003	-0.0955	-0.0209	-0.2495	5.2.4
C_n	-0.0007	0.0956	-0.0224	-0.9970	5.2.5
C_l	0.000	-0.0046	11.5022		5.2.6

Data from [4] were used as an initial comparison for the data results derived herein. Note that the data from [4] were acquired at higher Mach numbers. The lowest Mach number available was 0.6M which is considered to be at the high-end of the subsonic regime. Results from [4] were digitized and interpolated to the shoulder radius of the 1.8m MMEEV model. Pitching moment results were translated to the 0.214D location used for the B1R2 data run.

Results for static normal force (C_N) are provided in Figure 16. From this figure it can be seen that the Marko data exhibit a non-linearity for angles of attack less than ~6 degrees. There is no indication of this in the VST data as shown in Figure 12. Above ~6 degrees, the slopes of the two data sets are considered to be in reasonable agreement.

The comparison of static axial force results (C_A) is provided in Figure 17. Some of the differences between the two data sets can be attributed to the differences in Mach numbers with the Marko data potentially experiencing some transonic drag increase. Reynolds numbers for the two data sets were different with 1.0×10^6 for the Marko data and 0.24×10^6 for the VST data. An estimate of the drag rise effect at a Mach of 0.6 was acquired from [14] for the Viking entry vehicle and was approximately 5%. Applying this factor to the Marko data would improve the agreement between the two data sets. However the $\propto = 0$ results for C_A would indicate that the B1R2 results would still be approximately 4% lower than the Marko data.

Results for static pitching moment (C_m) are provided in Figure 18. From this figure it can be seen that there was excellent agreement between the two data sets. One concern regarding the comparison of the pitching moment results is that the Marko data are dependent on the pitching moment provided at the reference conditions as well as normal force which is required to translate the data to the 0.214D CM location. If the normal force was in poor agreement, it could be suggested that the pitching moment at the 0.214D location would also not be in good agreement for higher angles of attack. However, at 8 degrees angle of attack, the difference in C_m due to C_N was -0.029*-0.214=+0.0062. If the Marko C_N results were closer to the results for B1R2, then a larger difference between the C_m results would occur.

A comparison of the pitch and yaw damping results ($C_{m_q}$and C_{n_r}) were performed using data from the Viking entry vehicle as defined in [5]. The Viking entry vehicle was similar to, but somewhat different than the MMEEV considered herein. The Viking entry vehicle was a 70 degree sphere cone design with 0.25D nose radius and 0.007D shoulder radius. Extensive aerodynamic data were acquired for the Viking entry vehicle during the 1970s. Figure 19 shows the comparison of the data from the example MMEEV run (B1R2). To generate the MMEEV PID pitch and yaw damping model data, the angle of sideslip was set equal to the angle of attack for the C_{n_r} damping data. The elements of equations 5.2.14 that multiply $\hat{q}$ were taken as C_{m_q} (i.e., - 0.0208-0.2497*α^2) and similarly for C_{n_r}. From Figure 19 it can be seen that the MMEEV data approximates the Viking data at lower angles of attack. The MMEEV data does indicate an increase (i.e., more negative) damping with increasing angle of attack, but not as a significant rate of increase as the Viking data. This comparison is intended to provide an initial comparison and evaluation of the results from MMEEV data analysis effort.

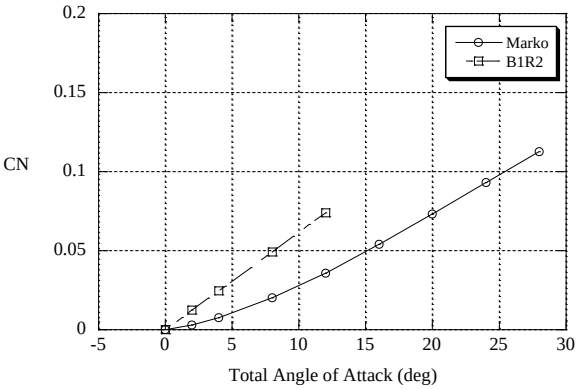

Figure 16 - Comparison of normal force coefficient.

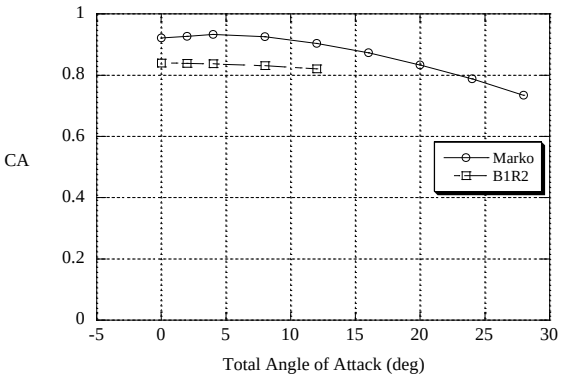

Figure 17 - Comparison of axial force coefficient.

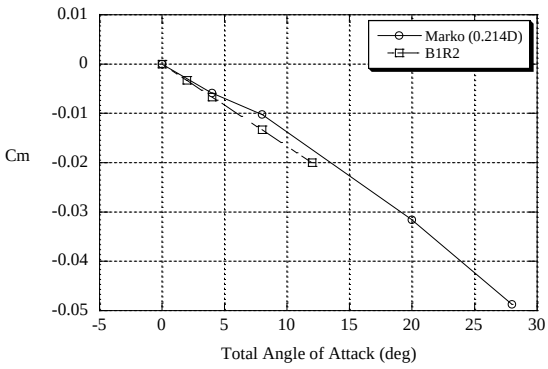

Figure 18 - Comparison of static pitching moment coefficient.

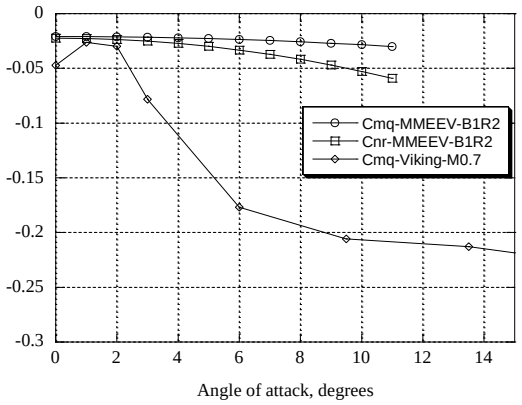

Figure 19 - Comparison of dynamic damping coefficients.

6. SUMMARY

Moving CM aft (from 0.214D to 0.234D) had a small observed effect on the model motions based on the unperturbed maximum total angle of attack data. From the perturbed data, indications are that the model has sufficient damping, both for the 0.214D and 0.234D CM locations to recover from total angles of attack up to approximately 70 degrees. Results also indicate slightly better damping for the aft CM. This result further indicates that the CM limit is well aft of the tested locations.

The 1.8m MMEEV demonstrates desirable stability during perturbations. For the 0.214D CM, perturbations up to 70 degrees were experienced with the model damping out the motions and returning to the nominal oscillations.

The effect of increasing inertia was significant with the oscillation amplitude increasing for the higher inertias. The amplitude of the oscillations of the 1.8m MMEEV for the 150% inertia case increased by a factor of 2 to 3 compared to the baseline inertia aft CM condition. Effective perturbation data were not acquired for this condition. As a result, it can be stated that the 0.214D CM and 150% inertia case is stable only up to ~29 degrees.

Comparison of the static and dynamic aerodynamic data from an example data run (B1R2) provided reasonable comparisons with data taken from [4]. Of all the comparisons (C_N,C_A,C_m, C_{m_q},C_{n_r}) the agreement of static pitching moment was considered excellent. Overall, more work fully processing and validating the results from the VST is considered required.

Future work will apply the PID tools developed to provide an aerodynamic database update to support MMEEV simulations. In addition, subsequent VST testing is planned that will provide data for an array of MMEEV outer mold lines.

7. ACKNOWLEDGEMENTS

The authors would like to acknowledge the contributions of Ashbee Sykes who provided a set of

Matlab PID scripts for processing the VST data. Dr Juan Cruz provided invaluable help regarding the verification of the data and analysis scripts as well as provided comparison reference data and review of this report.

8. REFERENCES

1. Mitcheltree, R.; Hughes, S.; Dillman, R.; Teter J.: *An Earth Entry Vehicle for Returning Samples from Mars,* 2nd International Symposium on Atmospheric Reentry Vehicles and Systems, Arcachon France, 2001.

2. Samareh, J. A., Maddock, R. W., and Winski, R. G., *An Integrated Tool for System Analysis of Sample Return Vehicles*, 2012 IEEE Aerospace Conference, Big Sky, Montana, March 3-10, 2012.

3. Mitcheltree, R.; Fremaux, C., Yates, Leslie: *Subsonic Static and Dynamic Aerodynamics of Blunt Entry Vehicles,* AIAA 99-1020.

4. Marko, Wayne J.: Static Aerodynamic Characteristics of Three Blunted Sixty-Degree Half-Angle Cones at Mach Numbers From 0.6 to 1.3. NASA TR-32-1298.

5. Steinberg, S.: Experimental Pitch Damping Derivative for Candidate Viking Entry Configurations at Mach Numbers from 0.6 thru 3.0, June 1970, Martin Marrieta Corporation.

6. Bowman, J. S., Dynamic Model Tests at Low Subsonic Speeds of Project Mercury Capsule Configurations with and without Drogue Parachutes, NASA TM X-459, 1961.

7. Bowman, J. S., Dynamic-Model Investigation of a 1/20-Scale Gemini Spacecraft in the Langley Spin Tunnel, NASA TN-D-2191, 1964.

8. Lee, H. A., and Burk, S. M., Low-Speed Dynamic Model Investigation of Apollo Command Module Configurations in the Langley Spin Tunnel, NASA TND-3888, 1967.

9. McCloy, R., Entry Dynamics Performance Predictions for Pioneer Venus Probes, AIAA-1978 1370, 1978.

10. Mitcheltree, R. A. and Fremaux, C. M., Subsonic Dynamics of Stardust Sample Return Capsule, NASA TM 110329, 1997.

11. Snow, W. L., Childers, B. A., Jones, S. B., and Fremaux, C. M.: Recent Experiences with Implementing a Video Based Six Degree of Freedom Measurement System for Airplane Models in a 20-Foot Diameter Vertical Spin Tunnel, Proceedings of the SPIE Videometrics Conference, Vol. 1820, 1992, pp. 158-180.

12. Wolowicz, Chester H.; Bowman, James S.; Gilbert, William R.: Similitude Requirements and Scaling Relationships as Applied to Model Testing. NASA TP-1435, August, 1979.

13. Klein, Vladislav; Morelli, Eugene A.: Aircraft System Identification Theory and Practice. AIAA 1801 Alexander Bell Drive, Reston, VA, 20191, 2006.

14. Flaherty, T.: Aerodynnamic Data Book VER-10, TR-3709014, Martin Marietta Corporation, June 1972.